Composition and non-equilibrium crystallization in partially devitrified co-rich soft magnetic nanocomposite alloys

P.R. Ohodnicki Jr. [a],[*], Y.L. Qin [a], D.E. Laughlin [a], M.E. McHenry [a], M. Kodzuka [b], T. Ohkubo [c], K. Hono [b],[c], M.A. Willard [d]

[a] *Materials Science and Engineering Department, Carnegie Mellon University, Pittsburgh, PA 15213, USA*
[b] *Graduate School of Pure and Applied Sciences, University of Tsukuba, Tenodai 1-1-1, Tsukuba 305-8571, Japan*
[c] *National Institute for Materials Science, 1-2-1 Sengen, Tsukuba 305-0047, Japan*
[d] *Multifunctional Materials Branch, Naval Research Laboratory, Washington, DC 20375, USA*

Abstract

The body-centered cubic (bcc) phase tends to preferentially nucleate during solidification of highly undercooled liquid droplets of binary alloy systems, including Fe–Co, Fe–Ni and Fe–Cr–Ni. We investigate a similar tendency during the partial devitrification of Co-rich amorphous precursors of composition $(Co_{1-x}Fe_x)_{88}Zr_7B_4Cu_1$ by identifying the structure and composition of the nanocrystalline grains. The Co:Fe ratio of the bcc nanocrystals varies linearly with the Co:Fe ratio of the amorphous precursor, and can lie well within the single-phase face-centered cubic (fcc) region of the Fe–Co phase diagram at the crystallization temperature. Classical nucleation theory therefore suggests several potential explanations for the preferential nucleation of bcc phase from an amorphous precursor, including: (i) a reduced amorphous/bcc interface energy as compared to the close-packed phases; (ii) a lower strain of precipitation for bcc nuclei as compared to close-packed fcc and hexagonal close-packed nuclei; and (iii) stabilization of the bcc phase by dissolved glass-formers such as Zr and B.
© 2008 Acta Materialia Inc. Published by Elsevier Ltd. All rights reserved.

Keywords: bcc Nanocrystalline materials; Crystallization; Three-dimensional atom probe (3DAP); Transmission electron microscopy (TEM)

1. Introduction

Preferential nucleation of a body-centered cubic (bcc) phase relative to a stable face-centered cubic (fcc) phase, as predicted by the bulk phase diagram, has been observed during the solidification of highly undercooled liquids in Fe–Co, Fe–Ni and Fe–Cr–Ni alloys [1–6]. Spaepen et al. [7,8] presented a theoretical model that predicts a lower interfacial free energy for solid–liquid interfaces of bcc crystals as compared to the fcc phase in most cases. The tendency for preferential nucleation of bcc phase was therefore rationalized using this interface energy model in the

context of classical homogeneous nucleation theory or diffuse interface theory as discussed by Kelly and Vander-Sande [9], Li et al. [1], Perepezko [10] and Volkmann et al. [2], for example. A similar tendency for preferential bcc phase nucleation has been observed during crystallization of some Fe–Ni–B- and Fe–Ni–Zr–B-based multicomponent amorphous precursors by Greer and Walker [11]. They assumed that the solubility of glass-formers in the crystalline phase was negligible and attributed the preferential nucleation of bcc phase in the multicomponent Fe–Ni amorphous alloys to the interfacial energy arguments used to explain this tendency in the highly undercooled liquids of simpler systems.

In our prior work [12], we also observed that the binary Fe–Co phase diagram generally underestimates the amount of bcc nanocrystalline phase observed after partial crystal-

---
[*] Corresponding author. Tel.: +1 412 973 4416.
   E-mail addresses: paul.ohodnicki@gmail.com, ohodnicki@ppg.com (P.R. Ohodnicki Jr.).

lization of Co-rich $(Co_{1−x}Fe_x)_{88}Zr_7B_4Cu_1$-based amorphous precursors. These observations are in agreement with the prior structural characterization studies of Willard et al. [13] on a $(Co_{0.95}Fe_{0.05})_{89}Zr_7B_4$ alloy with an Fe to (Fe + Co) ratio well within the single-phase fcc region of the binary Fe–Co phase diagram at the crystallization temperature. The preferential nucleation of bcc phase in a wide range of materials systems motivates us to perform a careful investigation of the composition of preferentially nucleated bcc nanocrystals in the more complex $(Co_{1−x}Fe_x)_{88}Zr_7B_4Cu_1$ and $(Co_{1−x}Fe_x)_{89}Zr_7B_4$ "nanocomposite" alloys. Because of the success of classical nucleation theory in explaining this phenomenon in the relatively simple undercooled liquids studied previously, we discuss the measured compositions in the framework of classical nucleation theory for the alloys under investigation here. We then compare the observations with predictions based on the binary Fe–Co phase diagram in an attempt to gain additional insight into the factors governing composition and phase selection of the nucleated nanocrystalline grains.

The $(Co_{1−x}Fe_x)_{88}Zr_7B_4Cu_1$-based alloys studied here are an example of a technologically relevant class of soft magnetic materials in which "nanocomposites" can be obtained consisting of nanocrystalline grains surrounded by an intergranular amorphous matrix. To obtain the "nanocomposite" microstructure, amorphous precursors of these compositions are produced by rapid solidification and subsequently annealed to promote partial crystallization during a primary crystallization reaction. This class of materials was born with the discovery of the five component Fe–Nb–Si–B–Cu alloy "FINEMET" by Yoshizawa et al. [14]. The discovery of simpler ternary or quaternary Fe–Zr–B–(Cu) alloys with similar microstructures soon followed [15]. The resultant materials exhibit combinations of high saturation induction and low core losses unobtainable in conventional amorphous or large-grained crystalline alloys. Co-substitutions, explored to increase saturation induction and improve properties of these alloys for high-temperature applications, led to the discovery of "HiT-Perm" alloys of composition $(Fe_{0.5}Co_{0.5})_{89}Zr_7B_4$ and $(Fe_{0.5}Co_{0.5})_{88}Zr_7B_4Cu_1$ [16,17]. More recently, a number of systematic investigations of the corresponding Co-rich alloys have been reported [12,13,18–23]. Co-rich alloys have been shown to demonstrate technologically interesting properties that include a dramatic response to magnetic field processing [18,19,24], high-temperature stability of magnetic properties [25–27] and superior ductility as compared with brittle Fe-based alloys [28]. Because the Co:Fe ratios of high Co-containing alloys correspond to the single-phase fcc region or the two-phase bcc + fcc region of the binary Fe–Co phase diagram, multiple nanocrystalline phases are possible, in contrast to the Fe-rich or near-equiatomic Fe–Co alloys, where bcc or CsCl-type ordered phases are clearly the most stable.

Here, we present a study of the composition of the nanocrystalline phases in three previously investigated alloys [12] spanning the transition from only bcc phase detectable

by X-ray diffraction (XRD) to multiple nanocrystalline phases. First, a structural characterization was performed using XRD, conventional transmission electron microscopy (CTEM) and high-resolution transmission electron microscopy (HRTEM) to identify the relevant phases present. The composition of each phase was then estimated by correlating three-dimensional atom probe (3DAP) analysis with the results of the structural characterization. The results of this study are compared with the predictions of the Fe–Co bulk phase diagram.

2. Experimental procedure

$(Co_{1−x}Fe_x)_{88}Zr_7B_4Cu_1$ amorphous ribbons with dimensions of ~3 mm width and ~30 μm thickness were synthesized by rapid solidification. The amorphous ribbons were isothermally annealed at 450 °C for 1 h to promote partial crystallization. The variable x corresponds to the Fe to (Fe + Co) ratio of the alloys in analogy with the mole fraction of Fe in a binary Fe–Co alloy. Values of $x = 0.15$, 0.10 and 0.04 were selected for investigation here because they span the transition from nucleation of a single bcc nanocrystalline phase to multiple nanocrystalline phases, as described in previous work [12,13] and illustrated in Fig. 1a. XRD was performed using a Philips X'Pert Thin Film Diffractometer with Cu Kα radiation, CTEM was performed with a JEOL 2000 microscope and HRTEM was performed for selected samples with a Tecnai F20 to identify the nanocrystalline phases. Samples for CTEM and HRTEM studies were prepared by ion milling using a Gatan Precision Ion Polishing System (PIPS). A locally built energy-compensated 3DAP equipped with the CAMECA's optical tomographic atom probe detector [29] was used to determine the average composition of the nanocrystals and intergranular amorphous phase for all compositions investigated. Needle-like specimens for the atom probe analysis were prepared by electropolishing the square rods of approximately 20 mm × 20 mm × 5 mm, which were prepared from the ribbon by mechanical grinding.

To provide additional confidence for the estimated compositions of the bcc nanocrystals and the proposed conclusions based upon these compositions, we also performed 3DAP for the $(Co_{0.95}Fe_{0.05})_{89}Zr_7B_4$ alloy crystallized at 450 °C for 1 h, as studied in Ref. [13]. For this sample, extensive structural characterization was performed and compositions were previously measured as reported in Refs. [13,30] using TEM-based techniques.

3. Results

XRD patterns obtained for the crystallized $(Co_{1−x}Fe_x)_{88}Zr_7B_4Cu_1$ ribbons with $x = 0.15$, $x = 0.10$ and $x = 0.04$ are shown in Fig. 1a. The major diffraction peaks are indexed to the bcc nanocrystalline phase despite having Co:Fe ratios which correspond to the two-phase α(bcc) + γ(fcc) or the single-phase γ(fcc) regions of the
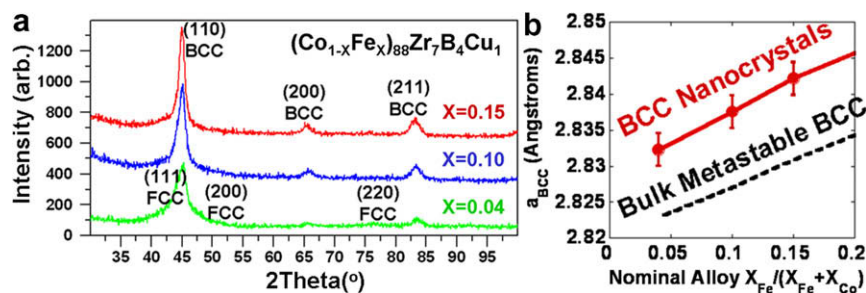
Fig. 1. (a) X-ray diffraction obtained for the $(Co_{1-x}Fe_x)_{89}Zr_7B_4Cu_1$ alloys with $x = 0.15$, 0.10 and 0.04 after annealing at $T = 450$ °C for 1 h to promote partial crystallization. (b) Lattice parameter of bcc nanocrystals calculated from the $(211)_{bcc}$ peak of (a) (solid line) and predicted lattice parameter (dashed line) from a metastable extension of bcc lattice parameter [31] using the actual Fe to (Fe + Co) ratio of the bcc nanocrystals from Table 1.

binary Co–Fe system [12]. For the $x = 0.04$ alloy, weak intensity peaks attributed to fcc nanocrystallites in our previous work [12] are also observed. The bcc phase lattice parameters derived from the $(211)_{bcc}$ peaks are presented in Fig. 1b. We note here that the lattice parameter of the bcc phase varies roughly linearly over this composition range and that it is larger than expected based on the extrapolations of the lattice parameter measured for the bcc phase in the bulk Fe–Co system. These features will be discussed in more detail in the context of 3DAP data below.

Bright field TEM images are presented in Fig. 2a–d for the $x = 0.10$ and $x = 0.04$ samples. The bright field images of Fig. 2a and b confirm a grain size of less than ~10 nm for both samples. In the selected area diffraction (SAD) pattern of Fig. 2c for the $x = 0.10$ sample, only evidence for a bcc nanocrystalline phase is observed. In the SAD pattern for the $x = 0.04$ sample (Fig. 2d), additional rings are observed that can be indexed to the fcc nanocrystalline phase.

HRTEM was performed for the annealed $x = 0.10$ and $x = 0.04$ samples to identify the phases of the nanocrystal-
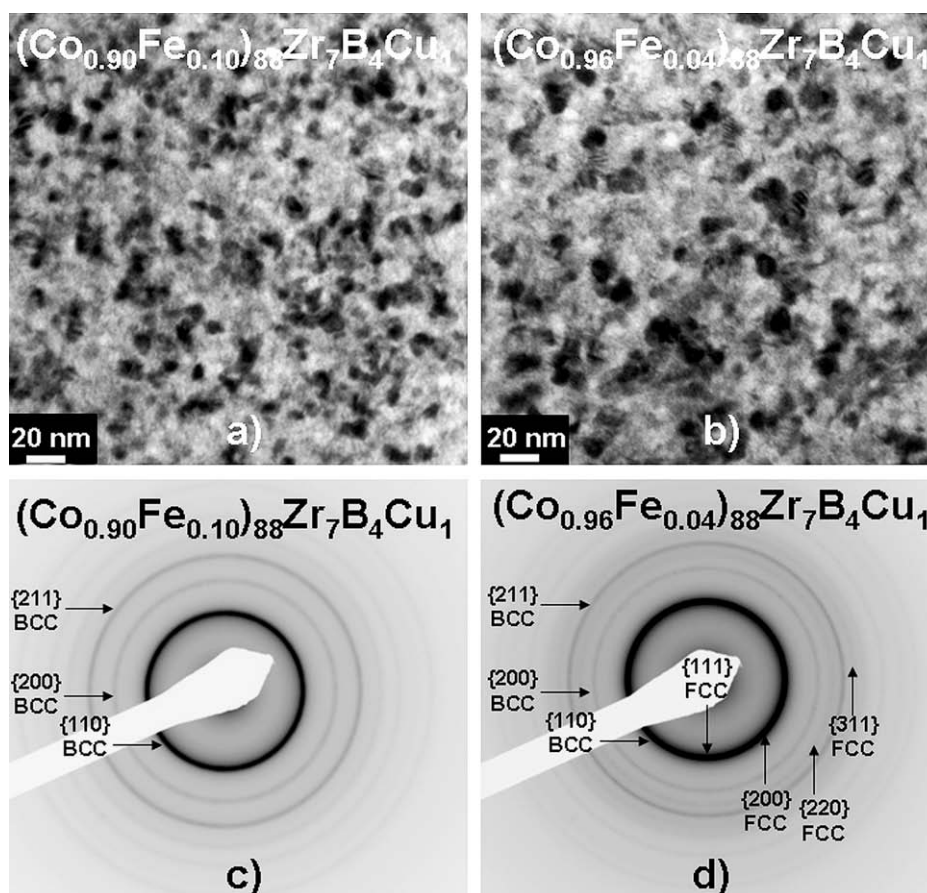

Fig. 2. Bright field TEM images of a $(Co_{0.90}Fe_{0.10})_{88}Zr_7B_4Cu_1$ alloy after annealing at $T = 450$°C for 1 h to promote primary crystallization (a) and the corresponding selected area diffraction pattern (c). Corresponding data for a $(Co_{0.96}Fe_{0.04})_{88}Zr_7B_4Cu_1$ alloy are shown in (b) and (d).

line grains. For the $x = 0.10$ sample, the majority of the grains were clearly indexed as the bcc phase, as expected from the XRD and SAD data presented for this sample above. However, a few exceptions were noted, including the observation of occasional fcc grains, as well as a few grains of an unknown non-cubic phase that could not be identified based on the fast Fourier transforms (FFTs) of the HRTEM images obtained. For the $x = 0.04$ sample, multiple nanocrystalline phases were observed in significant amounts, as expected. In addition to the bcc and fcc phases identified from XRD and SAD in Figs. 1a and 2d, hexagonal close-packed (hcp) grains that frequently contain a large number of stacking faults have also been observed by HRTEM for this composition. These observations are consistent with evidence for an hcp phase in the XRD patterns of the same sample ($x = 0.04$) after annealing at temperatures sufficiently high to crystallize the remaining intergranular amorphous matrix, as reported previously [12]. We have also identified clear evidence for hcp nanocrystals in XRD and SAD data not presented here for an Fe-free $Co_{89}Zr_7B_4$ alloy [32] and for an alloy with $x = 0.025$ [24].

In Fig. 3, nanocrystalline grains observed by HRTEM imaging for the $x = 0.04$ sample are presented, including a bcc grain (Fig. 3a), an fcc grain (Fig. 3b), an hcp grain with a relatively low density of stacking faults (Fig. 3c) and an hcp grain with a relatively high density of stacking faults (Fig. 3d). FFTs obtained from the grains in question and used to identify the nanocrystalline phase are also presented in Fig. 3. Note the significant streaking of the diffraction spots in the FFT of Fig. 3d along the normal direction to the close-packed planes $(0\,0\,1)_{hcp}$, due to a high density of stacking faults in this grain.

For completeness, we note that we have also identified regions in which nanocrystals with an orientation relationship are in intimate contact. In Fig. 4a, obtained for the $x = 0.10$ sample, two bcc nanocrystalline regions were observed to be separated by a $\{1\,1\,0\}$-type twin. In Fig. 4b, obtained for the $x = 0.04$ sample, two nanocrystalline regions are most appropriately indexed as bcc and fcc nanocrystals with a $(1\,1\,0)_{bcc}\|(1\,1\,1)_{fcc}$, $[1-1\,1]_{bcc}\|[1-1\,0]_{fcc}$ orientation relationship. However, the spots corresponding to the $(1\,1-1)$ and $(-1-1\,1)$ planes of the region indexed to the fcc phase are relatively weak in the FFTs. The lines indicating the approximate boundary between these nanocrystalline regions are indicated with dashed lines and the white arrows indicate the orientation of the spot shared by both regions in the overall FFTs. Because observations
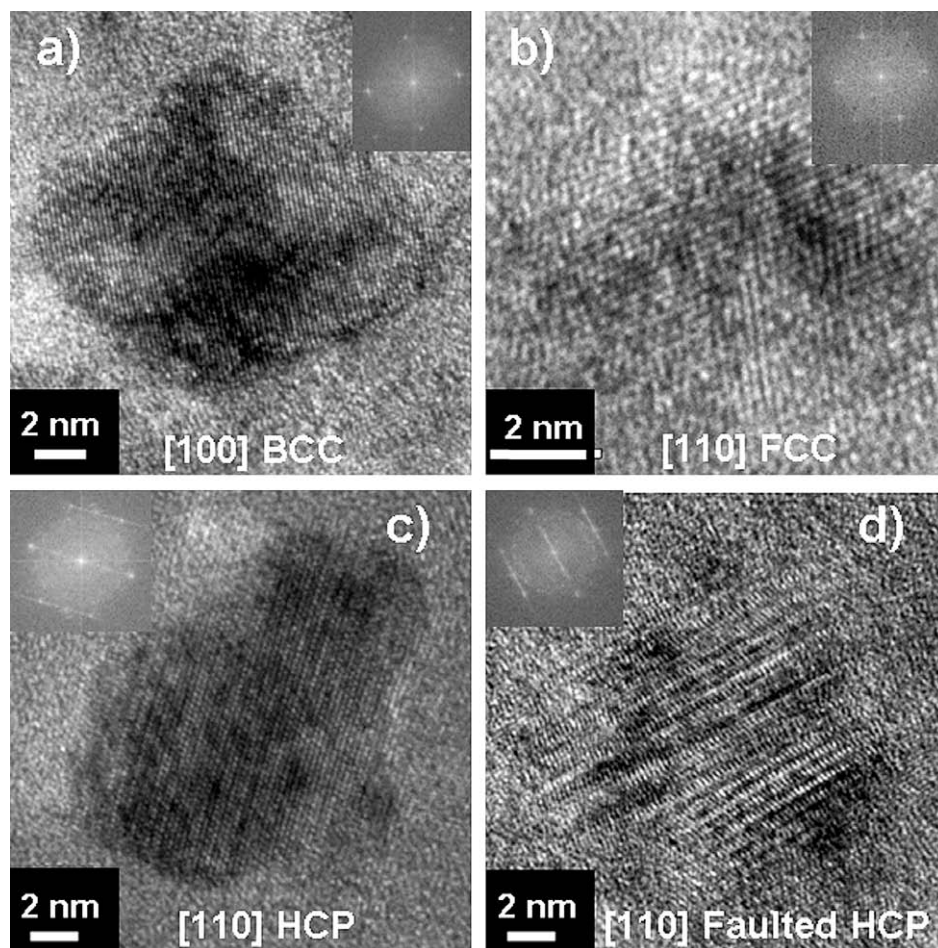

Fig. 3. Examples of nanocrystals observed through HRTEM imaging for the $(Co_{0.96}Fe_{0.04})_{88}Zr_7B_4Cu_1$ sample after annealing at $T = 450\,°C$ for 1 h to promote primary crystallization of the initially amorphous alloys. The insets are the FFTs used to identify the phase of the nanocrystals.
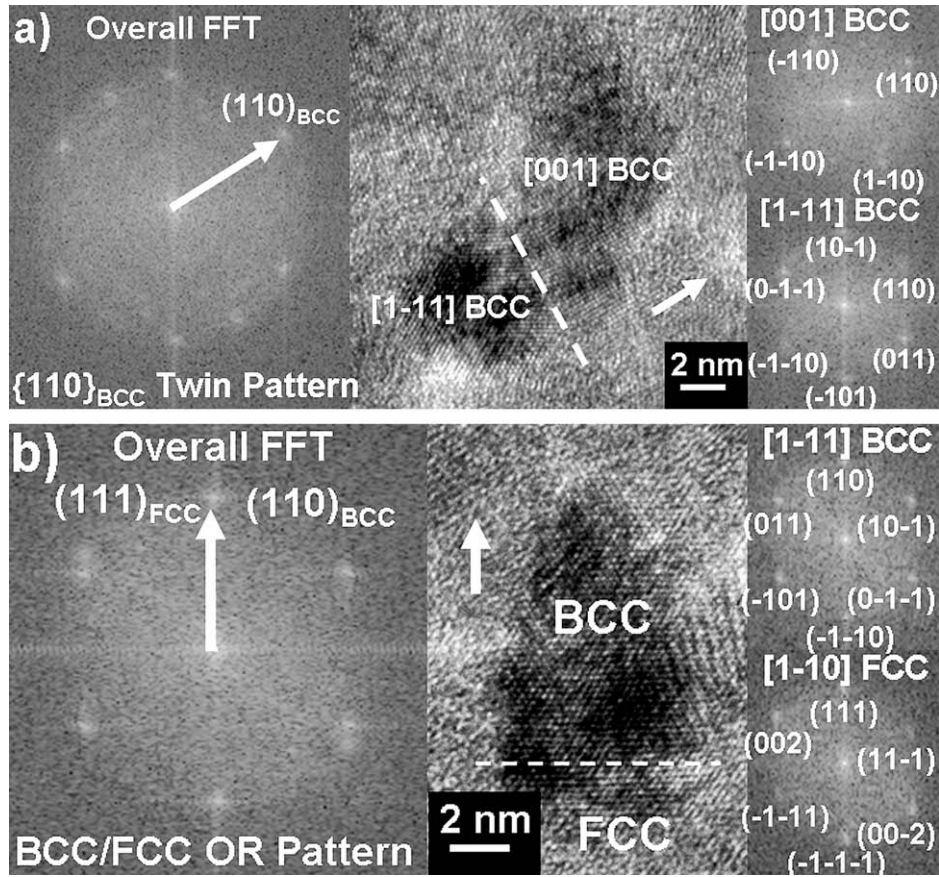
Fig. 4. Examples of HRTEM images (center) and FFTs (overall left, individual regions right) illustrating nanocrystalline regions in contact with orientation relationships. The white arrows in the FFTs of both sets of images indicate the spot shared by both nanocrystalline regions. (a) bcc regions separated by a {110}-type twin for the $(Co_{0.90}Fe_{0.10})_{88}Zr_7B_4Cu_1$ sample. (b) Regions most appropriately indexed to a bcc and an fcc region with an $(110)_{bcc}||(111)_{fcc}$, $[1-11]_{bcc}||[1-10]fcc$ orientation relationship for the $(Co_{0.96}Fe_{0.04})_{88}Zr_7B_4Cu_1$ sample.

such as those presented in Fig. 4 are relatively infrequent, they do not influence the main conclusions of this work as discussed below.

3DAP techniques were used to measure the composition of the phases present in the alloys investigated. Fig. 5 illustrates a map of the reconstructed atomic positions for the $x = 0.04$ alloy with multiple nanocrystalline phases present. The atom maps for the $x = 0.15$ and $x = 0.10$ samples (not shown for brevity) exhibit two regions, corresponding to: (i) nanocrystals enriched in Fe and depleted in Zr and B (Fe-rich, Zr-poor); (ii) an intergranular amorphous phase enriched in Zr, B and Cu (Fe-poor, Zr-rich). Because evidence for only bcc nanocrystalline phase is found in the XRD and SAD presented for these samples above (Figs. 1 and 2), the Fe-enriched crystallites corresponding to the Fe-rich and Zr-poor regions are identified as the bcc nanocrystalline phase.

For the $x = 0.04$ alloy, a third type of region is observed in the 3DAP maps corresponding to nanocrystals that are not enriched in Fe but are depleted in Zr, B and Cu with respect to the amorphous phase (Fe-poor, Zr-poor). These regions are attributed to the additional nanocrystalline phases present in this sample as detected by structural measurements. Because the free energies of the fcc and hcp
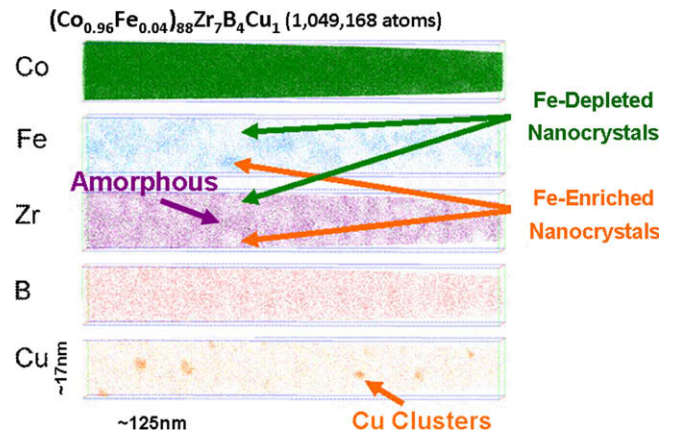

Fig. 5. 3DAP data illustrating Zr enrichment of the amorphous phase and Cu clustering as well as Fe-enriched and Fe-depleted nanocrystalline regions in the $(Co_{0.96}Fe_{0.04})_{88}Zr_7B_4Cu_1$ alloy. For the higher Fe-containing alloys, only Fe-enriched nanocrystals were observed.

phases are very similar for alloys rich in Co at the annealing temperatures used to crystallize the alloys, it is reasonable to expect the compositions of the fcc and hcp phases to be similar as well. Without additional information about the differences in composition between the various phases, we must therefore make the assumption that these regions

correspond to both the fcc and hcp nanocrystals. In Fig. 5, the three types of compositional regions are illustrated for the $x = 0.04$ alloy through a direct comparison of identical regions in the Zr and Fe maps.

Cu clustering is also observed in all of the Cu-containing alloys investigated here, as illustrated in Fig. 5. While Cu clusters play a critical role as heterogeneous nucleation agents for FINEMET alloys [14], the role of Cu as a nucleation agent in the case of Co-rich alloys is typically less important [13,22]. Our results support the conclusion that the density of Cu clusters is too small to account for the large number of nanocrystals observed. Thus, the tendency for the bcc phase to form cannot be attributed to a heterogeneous nucleation process at the location of Cu clusters. This is consistent with a tendency to form bcc phase at higher Co:Fe ratios than expected from the binary phase diagram even in the Cu-free alloys of this type [13].

Quantitative composition estimates were obtained from the full atom map for each alloy by coarse-graining the data into 300 atom cells. The composition of each cell was then calculated and binned according to the criteria illustrated in the appendix for each alloy based upon the three compositional regions discussed above (bcc nanocrystals = Fe-rich, Zr-poor; amorphous = Fe-poor, Zr-rich, B-rich; Fe-depleted nanocrystals = Co-rich, Fe-poor, Zr-poor). The composition of each binned collection was averaged to provide an average composition of the Fe-enriched bcc nanocrystals, the Fe-depleted nanocrystals and the intergranular amorphous phase. A volume fraction estimate is also obtained based on the number of each type of region observed. The results of this compositional analysis are summarized in Table 1. The nominal volume fractions add up to significantly less than 100% because a large number of the coarse-grained regions did not exhibit compositions that clearly fell into the threshold ranges. These "unknown regions" were not included in the calculations as they are not representative of the composition of any one of the phases of interest. Instead, they correspond primarily to regions that span across multiple phases, resulting in averaging of the compositions of different phases.

In addition to the $(Co_{1-x}Fe_x)_{88}Zr_7B_4Cu_1$ alloys of primary concern in this work, 3DAP data were obtained and analyzed for the $(Co_{0.95}Fe_{0.05})_{89}Zr_7B_4$ alloy crystallized at 450 °C for 1 h and investigated in previous works [13,30]. Only the bcc phase was identified in this sample based on the previously reported XRD and CTEM. This alloy is indicated by $x = 0.05$ in Table 1.

Based on the composition data of Table 1, the nanocrystalline phases for all of the alloys investigated have estimated Zr contents ranging between approximately 2.5% and 4.0% and B contents ranging between approximately 2% and 3%, which are larger than expected for the solubility of Zr and B into bulk bcc Fe or fcc Co [33]. Within experimental error, there is no evidence for a higher content of B and Zr atoms in the Fe-enriched bcc nanocrystals as compared with the Fe-depleted nanocrystals. For the $x = 0.04$ sample the total amount of the Fe-depleted nano-

crystalline phase is estimated to be about 10% by volume, while for the $(Co_{0.95}Fe_{0.05})_{89}Zr_7B_4$ sample only a small fraction of the regions ($<1\%$) can be classified in this way. For the $x = 0.10$ and $x = 0.15$ samples no evidence for Fe-depleted nanocrystals was found. The results are consistent with the corresponding structural measurements for these samples using XRD and CTEM.

The $(Co_{0.95}Fe_{0.05})_{89}Zr_7B_4$ alloy exhibits a much larger estimated volume fraction of remaining amorphous phase ($\sim 90\%$) as compared to the Cu-containing alloys ($\sim 50\%$). We attribute this difference to the close proximity of the annealing temperature (450 °C) to the primary crystallization temperature.

The average ratio of Fe to (Fe + Co) content in the nanocrystals and the amorphous phase were calculated from Table 1 and plotted as a function of the nominal Fe to (Fe + Co) content of the alloy in Fig. 6a. The expectations for a bulk binary alloy at equilibrium are presented for comparison and several important features of the resultant plot can be identified:

Observation #1: the Fe content of the bcc nanocrystals varies linearly with the Fe content of the precursor amorphous alloy.

Observation #2: the actual Fe to (Fe + Co) ratios of the bcc nanocrystallites are estimated to lie well within the two-phase region and at the extreme within the single-phase γ(fcc) region of the binary Fe–Co system.

Observation #1 is in sharp contrast to expectations for bulk, binary alloys in equilibrium as the Fe content of the bcc phase would be fixed at the value corresponding to the two-phase α(bcc) + γ (fcc) phase boundary. Because the bcc phase is the majority nanocrystalline phase for all alloys investigated here (see Table 1), Observation #2 indicates that the bcc phase is preferentially observed even for Fe to (Fe + Co) ratios for which the fcc phase would have a lower free energy in the binary Fe–Co system. To illustrate this, the Fe to (Fe + Co) ratio corresponding to the intersection of the free energy curves of the bcc and fcc phases (X_{T_0}, i.e., the T_0 line composition [34]) in the binary system are labeled in Fig. 6a as obtained from the 1998 public binary alloy database (PBIN) using the Thermo-Calc™ software package [35,36]. For clarity, X_{T_0} is represented schematically in Fig. 6b.

Using the measured Fe to (Fe + Co) ratios of the bcc nanocrystalline phases, the expected lattice parameters for metastable bulk Co–Fe alloys [31] were estimated to compare with the lattice parameters illustrated in Fig. 1b. The linear dependence of lattice parameter with nominal alloy composition is consistent with the linearly varying Fe to (Fe + Co) ratio and the slope is reasonably consistent with expectations for bulk binary Co–Fe alloys. The larger lattice parameter of the bcc nanocrystals relative to the bulk Co–Fe alloys of the corresponding Co:Fe ratio has been observed in other similar alloys and has been rationalized by the presence of the dissolved Zr and B in the nanocrystals [37]. These results indicate that the XRD and 3DAP results are consistent. It is noted that the composition data of Fig. 6a and lat-

Table 1
Results of full composition analysis for $(Co_{1-x}Fe_x)_{88}Zr_7B_4Cu_1$ alloys using 3DAP, calculated as described in the text using the threshold values listed in the appendix

$(Co_{1-x}Fe_x)_{88}Zr_7B_4Cu_1$ {NRL: $(Co_{0.95}Fe_{0.05})_{89}Zr_7B_4$} unit: at.%

Phase	X	Co	Fe	Zr	B	Cu	Volume	Volume (norm.)
Amorphous (Zr-rich, Fe-poor)	0.15	76.7	8.0	9.8	3.5	2.1	24.7	42.9
	0.10	80.0	5.2	9.2	3.7	1.9	23.5	49.7
	0.05	85.2	2.3	9.5	3.0	–	62.6	90.9
	0.04	83.3	1.6	9.8	3.3	2.1	35.5	57.3
bcc Nanocrystals (Fe-rich, Zr-poor)	0.15	75.1	18.4	3.0	2.7	0.9	32.9	57.1
	0.10	81.4	12.5	2.7	2.4	0.9	23.8	50.3
	0.05	86.0	7.1	3.9	2.9	–	5.8	8.4
	0.04	88.3	6.0	2.9	1.9	0.8	20.9	33.7
Fe-depleted nanocrystals (Co-rich, Fe-poor, Zr-poor)	0.15	–	–	–	–	–	–	–
	0.10	–	–	–	–	–	–	–
	0.05	91.9	1.9	3.3	2.8	–	0.5	0.7
	0.04	92.4	1.8	2.6	2.5	0.7	5.6	9.0

The compositions are listed in at.% and the nominal and normalized volume fractions of each phase are presented as well. The values obtained here for a $(Co_{0.95}Fe_{0.05})_{89}Zr_7B_4$ ($x = 0.05$) sample synthesized and characterized at the Naval Research Laboratories in previous works are also presented for comparison [13,30].
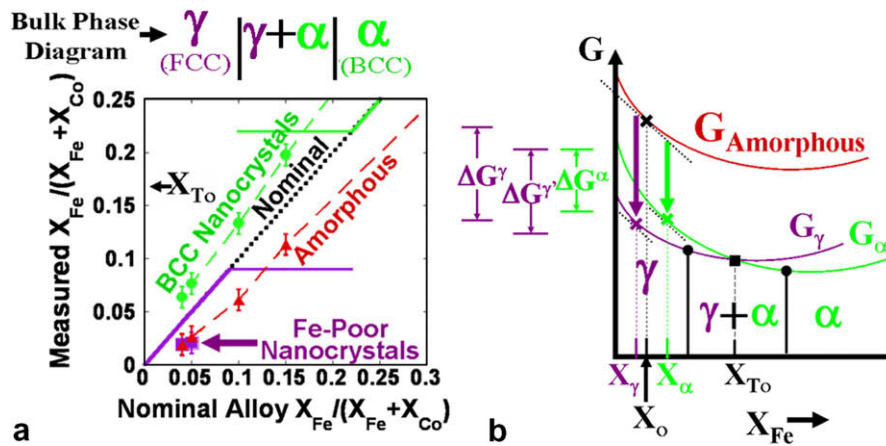

Fig. 6. (a) Measured Fe to (Fe + Co) ratio vs. nominal alloy composition (dashed lines) and comparison with expectations for bulk Fe–Co alloys in equilibrium at $T = 450\ °C$ (solid lines). The $(Co_{0.95}Fe_{0.05})_{89}Zr_7B_4$ sample synthesized at the Naval Research Laboratories corresponds to $x = 0.05$. (b) Schematic free energy curves for the amorphous, α(bcc) and γ(fcc) phases of Co-rich binary Fe–Co alloys at $T = 450\ °C$. X_0 = initial amorphous alloy composition, X_α = composition that maximizes the driving force for nucleation of the α-phase (ΔG^α), X_γ = composition that maximizes the driving force for nucleation of the γ-phase (ΔG^γ), and X_{T_0} is the composition corresponding to the intersection of the free energies of the α(bcc) and γ(fcc) phases. The primed ΔG^γ is the driving force for nucleation of the γ-phase of composition X_α, which is larger than ΔG^α because $X_\alpha < X_{T_0}$.

tice parameter data of Fig. 1b are extrapolated to the published value for the well-known HiTPerm composition of $(Fe_{0.5}Co_{0.5})_{88}Zr_7B_4Cu_1$ [37] and measured for an alloy synthesized by us, respectively.

4. Discussion

In this section, we briefly and qualitatively discuss the observations outlined above in terms of classical homogeneous nucleation theory for a binary system. A more thorough discussion can be found in Ref. [24] and in a planned publication which is currently underway. This model is clearly an oversimplification of the true situation in these complex alloy systems. However, the ability of the model to reasonably account for preferential nucleation of bcc in the liquid droplet experiments of the simpler Fe–Co, Fe–Ni and Fe–Cr–Ni systems suggests that it may be a use-

ful starting point for understanding the more complex system investigated here.

In the framework of classical nucleation theory, as discussed in Refs. [38–40], for example, the composition and phase of the nucleus with the highest probability to form is assumed to be the one that minimizes the activation barrier to nucleation [2,10,11]. The activation barrier for nucleation, ΔG_β^*, is expressed in Eq. (1) for a spherical nucleus of β-phase precipitating from a parent δ-phase:

$$\Delta G_\beta^* = \frac{16\pi\sigma_{\delta,\beta}^3}{3(\Delta G^\beta + W^{\delta,\beta})^2} \quad (1)$$

where $\sigma_{\delta,\beta}$ is the interfacial free energy between the parent and product phases, $W^{\delta,\beta}$ is the strain energy of the precipitate-matrix system and ΔG^β is the thermodynamic driving force for nucleation. Assuming that the interfacial energy and strain terms are sufficiently similar in the two phases,

the phase that minimizes ΔG_{β}^{*} is the one that maximizes the thermodynamic driving force, ΔG^{β}. If this assumption is not true, then all three of these terms must be considered.

At a given temperature, ΔG^{β} is determined by the composition dependence of the free energies of the bulk phases. For the first nucleus to precipitate in a binary system, ΔG^{β} is determined as a function of composition from the free energy curves of the parent and product phases. Fig. 6b shows ΔG^{β} to be the vertical distance between the line tangent to the parent phase at the initial composition and the free energy of the product phase evaluated at the composition of the nucleus. The value of ΔG^{β} is maximized at the product phase composition where the slope of the free energy curve of the product phase is equal to that of the parent phase at the original composition shown in Fig. 6b [41]. This "parallel tangency" condition is different from the "common tangency" condition that dictates phase equilibria in binary systems. For example, the Fe:Co ratio of the bcc phase that satisfies the "parallel tangency" condition varies monotonically with the nominal alloy Fe:Co ratio even if multiple phases are nucleating. In contrast, the "common tangency" condition fixes the Fe:Co ratio of the bcc phase in a two-phase region. If maximization of the thermodynamic driving force (ΔG^{β} of Eq. (1)) is dictating the composition of the nucleated phase, then the composition that satisfies the "parallel tangency" condition is also the most probable nucleus composition to form. These simple arguments illustrate that there is a difference between the conditions dictating the composition of the first nucleus to form and the conditions that dictate the compositions of the bcc and fcc phases that minimize the free energy in equilibrium. This difference explains the observed monotonic trend in the Fe to (Fe + Co) ratio of the bcc nanocrystals that correspond to the two-phase region of the bulk Fe–Co system, as shown in Fig. 6a.

A detailed understanding of the compositional dependence of the free energies of the various phases is required in order to use classical nucleation theory to predict the most probable identity and composition of the phase to nucleate first at a given temperature. However, at a fixed product phase composition, the phase with the highest driving force for nucleation has the lowest free energy, independent of the free energy of the parent phase. Thus, for a binary alloy, if the composition of the product phase is known with respect to the intersection of the free energy curves at a given temperature, X_{T_0}, the phase with the maximum driving force for nucleation can be determined unambiguously. For partitionless nucleation, the compositions of the parent and product phases are the same, making comparison of the parent phase composition to X_{T_0} strictly valid. For transformations in which the composition of the product phase differs from that of the parent phase, the composition of the product phase (and not the parent phase) must be considered.

Based on maximizing the thermodynamic driving force for the bcc phase, the origin of bcc phase preferential nucleation was first suggested to be Fe enrichment of the nanocrystalline bcc phase in Ref. [13]. In our data (Fig. 6a), partitioning of Fe to the nanocrystalline phase resulting in Fe enrichment is observed. However, the measured Fe to (Fe + Co) ratios of the majority bcc phase nanocrystals are well beyond the estimated composition of the free energy curve intersection, X_{T_0}, at the annealing temperature used to crystallize these alloys. We therefore conclude that maximization of the thermodynamic driving force for nucleation through partitioning of Fe to the nanocrystalline bcc phase is not sufficient to explain preferential nucleation of the bcc phase.

In the framework of classical homogeneous nucleation theory, Eq. (1), other reasons for preferential nucleation of a bcc nanocrystalline phase from the amorphous phase can be proposed:

(1) There may be a lower interfacial energy of the amorphous–solid interface for bcc crystals analogous to the lower estimated interfacial energy of the liquid–solid interface in Fe–Co, Fe–Ni and Fe–Cr–Ni alloys, as discussed in the introduction. This is the argument presented by Greer and Walker [11] in the context of crystallization of Fe–Ni-based amorphous alloys.
(2) A lower strain energy associated with formation of a critical nucleus of the bcc phase relative to the fcc or hcp phases [42] is expected, as discussed in Ref. [24]. This effect is unique to crystallization from amorphous solids when compared with solidification from a highly undercooled liquid.
(3) The significant content of dissolved Zr and B in the nanocrystalline phase (roughly 2–4 at.% of each) could stabilize bcc relative to the close-packed fcc and hcp. However, no experimentally significant tendency for partitioning of Zr or B to the Fe-enriched bcc nanocrystalline regions relative to the Fe-depleted nanocrystalline regions was observed here.

Since the interface energy and strain terms are general for cases in which bcc and close-packed structures such as fcc and hcp are competing phases, the first two factors would tend to promote preferential nucleation of bcc in a wide range of alloy compositions. The situation would be analogous to the tendency for preferential nucleation of bcc phase observed in the droplet nucleation experiments of highly undercooled Fe–Co, Fe–Ni and Fe–Ni–Cr liquids. The latter, however, would be expected to depend more strongly upon the glass-former elements, such as Si, Zr, Nb and B. As a result, the situation is more complex in the class of materials under investigation here than the simpler systems for which similar observations have been reported.

5. Conclusions

We have characterized a number of Co-rich $(Co_{1-x}Fe_x)_{88}Zr_7B_4Cu_1$ alloys using XRD, CTEM, HRTEM and 3DAP techniques, and observed in them a tendency for the bcc phase to nucleate preferentially. Through HRTEM imaging, bcc, fcc and hcp phases were all observed for the highest Co-containing sample and infrequent evidence for nanocrystalline regions in intimate contact with orientation relation-

ships was noted, namely bcc regions separated by a {110}-twin and bcc/fcc regions with orientation relationships. The composition of the preferentially nucleated bcc nanocrystalline phase varies monotonically with the corresponding ratio of the amorphous precursor and can lie well within the two-phase α(bcc) + γ(fcc) region or the single-phase γ(fcc) region of the binary Fe–Co phase diagram for the highest Co-containing alloys. Based on these measured compositions, classical homogeneous nucleation theory would suggest that one or more of the following factors are responsible for the preferential nucleation of bcc phase: (i) a lower crystalline–amorphous interfacial energy of the bcc nuclei; (ii) a lower precipitate–matrix strain energy for bcc nuclei as compared to the close-packed fcc and hcp phases; (iii) stabilization of the bcc phase by dissolved glass-former species. For crystallization of this genre of complex multicomponent amorphous solids, the situation is complicated compared to the highly undercooled liquids, for which the analogous tendency for the bcc phase to nucleate has been observed and explained by the reduced solid/liquid interface energy of bcc crystals compared to fcc or hcp crystals.

Acknowledgements

Appendix

Threshold values used to obtain the compositional data presented in Table 1

$(Co_{1-x}Fe_x)_{88}Zr_7B_4Cu_1$ {NRL: $(Co_{0.95}Fe_{0.05})_{89}Zr_7B_4$} unit: at.%

Phase	X	Co	Fe	Zr	B	Cu
Amorphous (Zr-rich, Fe-poor)	0.15	–	<13.0	>7.0	–	<4.0
	0.10	–	<10.0	>7.0	–	<4.0
	0.05	–	<5.0	>7.0	–	<4.0
	0.04	–	<4.0	>7.0	–	<4.0
bcc Nanocrystals (Fe-rich, Zr-poor)	0.15	–	>14.5	<6.0	–	<3.0
	0.10	–	>10.5	<6.0	–	<3.0
	0.05	–	>6.5	<6.0	–	<3.0
	0.04	–	>4.5	<6.0	–	<3.0
Fe-depleted nanocrystals (Co-rich, Fe-poor, Zr-poor)	0.15	–	–	–	–	–
	0.10	–	–	–	–	–
	0.05	>90	<4.0	<4.0	–	<1.5
	0.04	>90	<3.0	<4.0	–	<1.5

References

[1] Li M, Ozawa S, Kuribayashi K. Phil Mag Lett 2004;84:483.
[2] Volkmann T, Herlach D, Löser W. Metall Mater Trans A 1997;28:453.
[3] Eckler K, Gartner F, Assadi H, Norman AF, Greer AL, Herlach DM. Mater Sci Eng A 1997;226–228:410.
[4] Li M, Yang G, Zhou Y. J Mater Sci 2000;35:3069.
[5] Yeon-Wook K, Hong-Ming L, Kelly TF. Acta Metall 1988;36:2525.
[6] Hong-Ming L, Yeon-Wook K, Kelly TF. Acta Metall 1988;36:2537.
[7] Spaepen F. Acta Metall 1975;23:729.
[8] Spaepen F, Meyer RB. Scripta Metall 1976;10:37.
[9] Kelly TF, VanderSande JB. Int J Rapid Solidification 1987;3:51.
[10] Perepezko JH. Mater Sci Eng A 2005;413–414:389.
[11] Greer AL, Walker IT. Mater. Sci. Forum 2002;386–388:77.
[12] Ohodnicki PR, Park SY, McWilliams HK, Ramos K, Laughlin DE, McHenry ME. J Appl Phys 2007;101:09.
[13] Willard M, Heil T, Goswami R. Metall Mater Trans A 2007;38:725.
[14] Yoshizawa Y, Oguma S, Yamauchi K. J Appl Phys 1988;64:6044.
[15] Makino A, Suzuki K, Inoue A, Masumoto T. Mater Trans JIM 1991;32:551.
[16] McHenry MA, Willard ME, Laughlin DE. Prog Mater Sci 1999;44:291.
[17] Willard MA, Laughlin DE, McHenry ME, Thoma D, Sickafus K, Cross JO, et al. J Appl Phys 1998;84:6773.
[18] Yoshizawa Y, Fujji S, Ping DH, Ohnuma M, Hono K. Scripta Mater 2003;48:863.
[19] Yoshizawa Y, Fujji S, Ping DH, Ohnuma M, Hono K. Mater Sci Eng A 2004;375–377:207.
[20] Yoshizawa Y, Bizen Y, Yamauchi K, Nishiyama T, Suwabe S. Soft magnetic alloy with ultrafine crystal grains and method of producing the same, vol. 5151137. United States of America: Hitachi Metals Limited; 1992.
[21] Yoshizawa Y. Co-based magnetic alloy and magnetic members made of the same, vol. 6648990 B2. United States of America: Hitachi Metals Limited; 2003.
[22] Ohnuma M, Ping DH, Abe T, Onodera H, Hono K, Yoshizawa Y. J Appl Phys 2003;93:9186.
[23] Heil TM, Willard MA, Flores JJ. J Appl Phys 2007;101:09N107.
[24] Ohodnicki PR. PhD Thesis. Materials Science and Engineering Department, Carnegie Mellon University; 2008.
[25] Daniil M, Willard MA. J Appl Phys 2008;103:07E727.
[26] Willard MA, Francavilla T, Goswami R, Harris VG. Mater Res Soc Symp Proc 2005;851:NN5.2.1.
[27] Blazquez JS, Conde CF, Franco V, Conde A, Kiss LF. J Appl Phys 2008;103:07E721.
[28] Heil TM, Wahl KJ, Lewis AC, Mattison JD, Willard MA. Appl Phys Lett 2007;90:212508.
[29] Deconihout B, Renaud L, Costa GD, Bouet M, Bostel A, Blavette D. Ultramicroscopy 1998;73.
[30] Goswami R, Willard MA. Scripta Mater 2008;59:459–62.
[31] Ellis WC, Greiner ES. Trans ASM 1941;29:415.
[32] Ohodnicki JPR, Keylin V, McWilliams HK, Laughlin DE, McHenry ME. J Appl Phys 2008;103:07E740.
[33] Binary alloy phase diagrams. Materials. Park, OH: ASM International; 1990.
[34] Massalski TB. Proceedings of 4th international conference on rapidly quenched metals. Sendai: The Japan Institute of Metals; 1981. p. 203.
[35] Guillermet AF. TRITA-MAC 1986;324.
[36] Guillermet AF. High Temp High Pres 1988;19:477.
[37] Ping DH, Wu YQ, Hono K, Willard MA, McHenry ME, Laughlin DE. Scripta Mater 2001;45:781.
[38] Turnbull D. J Appl Phys 1950;21:1022.

[39] Cahn RW, Haasen P, Kramer EJ. Materials science and technology: a comprehensive treatment. Weinheim: Wiley-VCH; 2005.

[40] Aaronson H. Lectures on the theory of phase transformations. New York: The Metallurgical Society of AIME; 1975.

[41] Hillert M. Lectures on the theory of phase transformations. In: Aaronson HI, editor. Civilization and culture. Warrendale, PAS: The Minerals, Metals, & Materials Society; 1999. p. 10–20.

[42] Nabarro FRN. Proc Royal Soc Lond 1940;175:519.